Liposome encapsulated polydopamine nanoparticles: Enhancing ferroptosis and activating hypoxia prodrug activity

Yijun Guo [a,1], Huiling Luo [a,1], Hairong Jiang [b], Xinxin Liu [a], Xinrui Long [a], Yinuo Hou [b], Zhou Chen [a,*], Yanan Sun [a], Dongtao Ge [a,**], Wei Shi [a,***]

[a] The Higher Educational Key Laboratory for Biomedical Engineering of Fujian Province, Fujian Key Laboratory of Surface and Interface Engineering for High Performance Materials, Department of Biomaterials, College of Materials, Xiamen University, Xiamen 361005, Fujian, China
[b] College of Chemistry and Chemical Engineering, Xiamen University, Xiamen 361005, Fujian, China

ABSTRACT

The short lifespan of active oxygen species and depressed O_2 level during ferroptosis treatment in tumor cells weaken ferroptosis therapy. How to improve the utilization efficiency of active oxygen species generated in real time is pivotal for anticancer treatment. Herein, the tirapazamine (TPZ) loaded polydopamine-Fe nanoparticles (PDA-Fe-TPZ) was modified with unsaturated liposome (Lip), which was constructed to overcome the drawbacks of traditional ferroptosis therapy. The Lip@PDA-Fe-TPZ nanoliposomes can react with H_2O_2 to produce •OH by Fenton reaction, which then attacks Lip and transforms into radical intermediate (L•) and phospholipid peroxide radical (LOO•) to avoid the annihilation of •OH. The introduced Lip enhances lipid peroxidation and promotes oxygen consumption, resulting in increased hypoxia at tumor site. The introduced TPZ can be triggered by reductase in tumor cells under hypoxia, which can reduce to transient oxidative free radicals by reductase enzymes and destroy the structure of the surrounding biomacromolecules, thus achieving the synergistic treatment of ferroptosis and chemotherapy. In this work, we organically combined enhanced ferrroptosis with hypoxic activated chemotherapy to achieve efficient and specific tumor killing effect, which can sever as a promising treatment of cancer in the future.

1. Introduction

Cancer is still a major problem plaguing human life and health. The therapeutic efficacy of traditional treatment methods, such as chemotherapy, radiotherapy and surgery, are still not satisfactory, and the side effects are more damaging to the human body [1–3]. The development of treatment strategies that can effectively induce tumor cell death is a goal that people have been pursuing. Ferroptosis is a programmed cell death caused by iron-dependent lipid peroxides accumulation, which has attracted great attention as an emerging tumor therapy [4–6]. The Fe ions (ferrous (Fe^{2+}) or ferric (Fe^{3+}))-mediated Fenton reaction converts endogenous H_2O_2 into strong cytotoxicity hydroxyl radicals (•OH). The high level of •OH in the cell leads to an excess of lipid peroxide (LPO) on the cell membranes, then triggers and completes ferroptosis in tumor cells [7–10]. Recently, tumor therapy based on ferroptosis has a

good prospect in inducing cancer cell death due to its characteristics of high tumor specificity and low systemic side effects [11–13]. However, due to the short half-life (<1 ns) and easy annihilation of •OH, it is difficult to fully trigger lipid peroxidation. The low •OH utilization rate has become the main bottleneck restricting the therapeutic efficacy of ferroptosis [14]. Unfortunately, the existing research cannot provide an effective strategy to improve the •OH utilization rate. Therefore, it is urgent to construct an efficient tumor treatment strategy based on ferroptosis.

Inspired by lipid peroxidation in living systems, our group has designed a •OH/LPO nano-converter to trigger •OH into LPO at Fenton reaction sites, and this strategy has been proved that can improve the utilization rate of •OH and enhance tumor ferroptosis [15]. In this case, •OH attacks on unsaturated liposomes (Lip) to trigger lipid peroxidation, which is the downstream executor of ferroptosis induction.

Specifically, •OH produced by Fenton reaction attacks Lip *in situ* to form phospholipid radical L•. L• can be converted to lipid peroxyl radical (LOO•) and lipid hydroperoxide (LOOH) with the participation of oxygen molecules [14,16,17]. In addition, new LOOH would be further generated in the presence of Fe^{2+} and Fe^{3+}. Therefore, the chain reaction of lipid peroxidation can not only avoid the annihilation of •OH, but also achieves the accumulation of lipid peroxides, which will improve the efficiency of ferroptosis. This process occurs in tumor cells could improve the efficacy of ferroptosis due to the intensive activation of lipid peroxidation [18–22]. However, we notice that lipid peroxidation consumes oxygen, which makes the hypoxic tumor microenvironment even worse [23–26]. Tumor hypoxia induces apoptosis and expression of autophagy-related genes, and chemotherapy resistance occurs, leading to malignant phenomena such as tumor proliferation and invasion [27–30]. How to turn this side effect into an advantage is important to further enhance the efficiency of tumor treatment. Herein, we planned to develop a new strategy to enhance tumor treatment combined with ferroptosis in this hypoxic tumor microenvironment.

Hypoxic activated prodrugs (HAPs) have attracted increasing attention and have been widely used in tumor synergistic therapy [31–34]. HAPs can be triggered by reductase in hypoxic tumor cells to generate free radical metabolites, but has no toxic effect on normal tissues or cells [35–38]. For example, Zhang *et al.* provided a new strategy: photosensitizer enhanced HAPs activation inhibits glioma growth by encapsulating tirapazamine (TPZ) as a HAP and zinc phthalocyanine (ZnPc) as a photosensitizer to enhance hypoxia [39]. After being internalized by tumor cells and radiated by laser, ZnPc can not only efficiently consume intratumoral O_2 to produce reactive oxygen species (ROS) for achieving photodynamic therapy, but also aggravate hypoxia to activate TPZ for amplifying chemotherapy, which ultimately inhibits tumor growth. Therefore, using HAPs to convert the side effects of lipid peroxidation enhanced hypoxia into activation of chemotherapy

is a promising approach for tumor combination therapy.

In this paper, a polydopamine (PDA) delivery system loaded with iron ions and TPZ (PDA-Fe-TPZ), was synthesized by one-pot method. Then Lip@PDA-Fe-TPZ nanoliposomes were successfully prepared by modifying PDA-Fe-TPZ with Lip. The synthesis process and action mechanism are shown in Scheme 1. Nanoparticles with iron ions reacted with H_2O_2 in tumor cells and produced •OH by Fenton reaction. •OH can attack Lip to result in lipid peroxidation cascade reaction to achieve the propagation of reactive oxygen species (ROS) and accumulation of lipid peroxides, which further strengthening ferroptosis effect. In addition, the consumption of oxygen in tumor cells activates the hypoxia-activated chemotherapy, which can significantly enhance the antitumor therapeutic efficiency by integrating advantages of ferroptosis and chemotherapy.

2. Results and discussion

2.1. Characterization of Lip@PDA-Fe-TPZ

One-pot process was used to synthesize the PDA delivery carriers loaded with iron ions and hypoxia-activated prodrug TPZ. The scanning electron microscope (SEM) and transmission electron microscope (TEM) images of PDA-Fe (Figure S1A) and PDA-Fe-TPZ (Fig. 1A and Figure S1C) showed that both nanoparticles exhibited uniform spherical with a particle size about 110 nm. Loading with small molecule prodrug TPZ into PDA-Fe does not change the morphology and size of nanoparticles. Then, the PDA-Fe and PDA-Fe-TPZ were modified by unsaturated Lip to prepare Lip@PDA-Fe and Lip@PDA-Fe-TPZ, respectively. The Lip coating on the surface of Lip@PDA-Fe (Figure S1B) or Lip@PDA-Fe-TPZ (Fig. 1B and Figure S1D) can be clearly observed in SEM and TEM images. We used thermal gravimetric analysis (TGA) to calculate the content of the Lip in Lip@PDA-Fe-TPZ (Figure S2), and the Lip
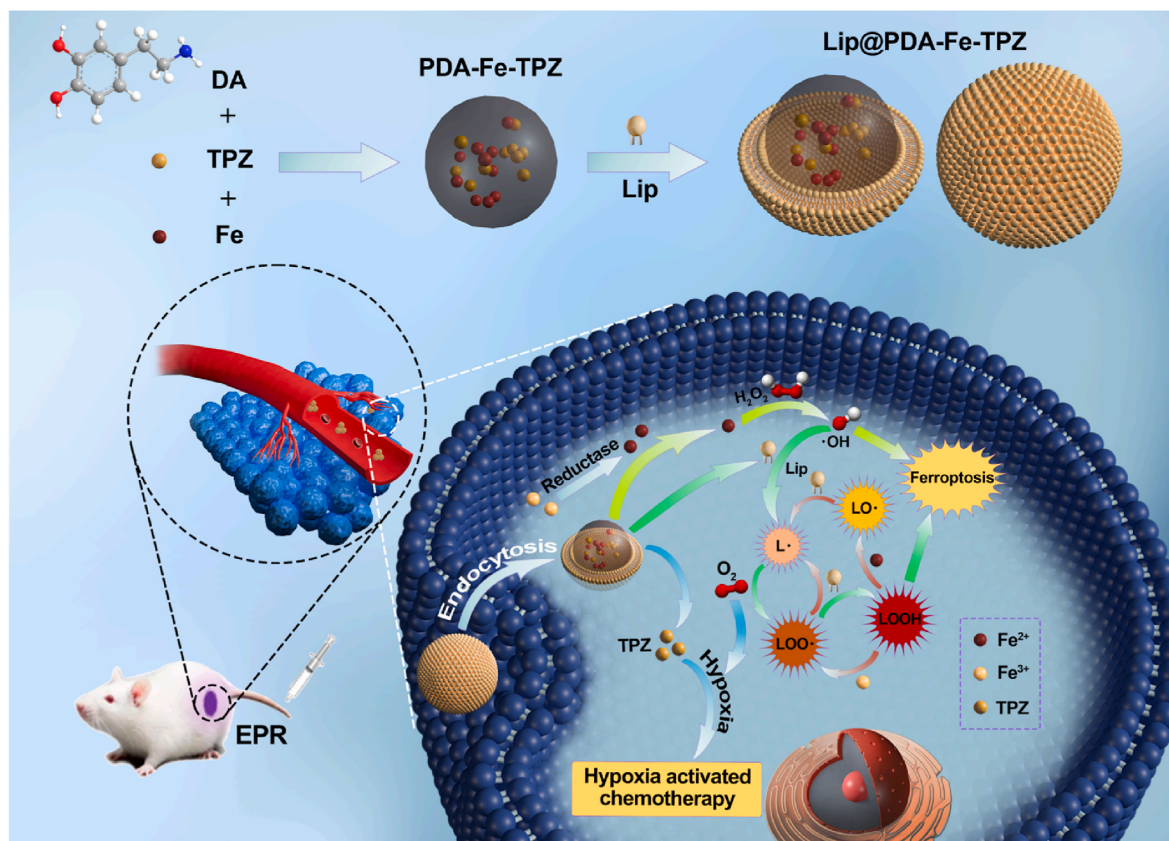
Scheme 1. The synthesis of Lip@PDA-Fe-TPZ and the mechanism of enhancing ferroptosis and activating chemotherapy to antitumor treatment.
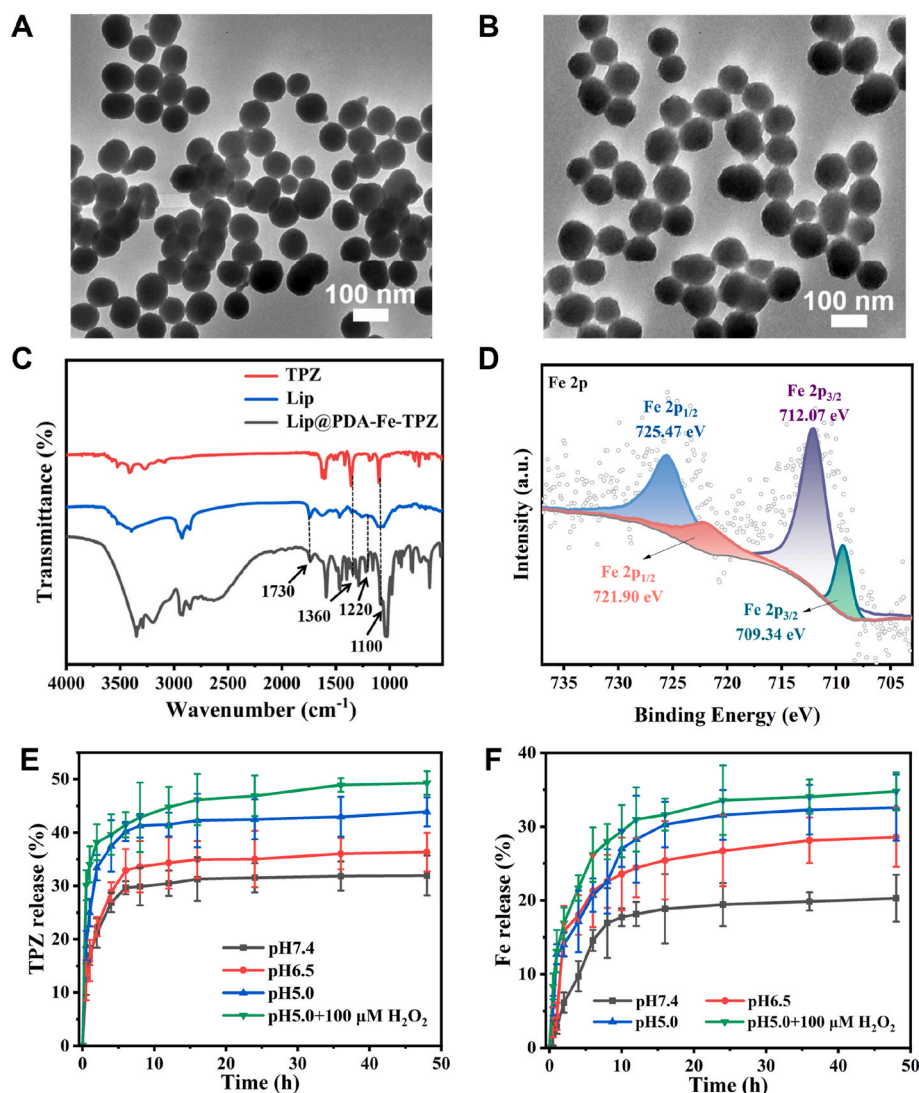
Fig. 1. Characterizations of the Lip@PDA-Fe-TPZ nanoliposomes. TEM images of PDA-Fe-TPZ (A) and Lip@PDA-Fe-TPZ (B); FTIR spectra (C) and Fe 2p XPS spectra of the Lip@PDA-Fe-TPZ nanoliposomes (D); TPZ (E) and Fe ion (F) release profiles from the Lip@PDA-Fe-TPZ nanoliposomes in different mimicking environment.

content is about 7.28 wt%. Dynamic light scattering (DLS) results showed that the diameter of Lip@PDA-Fe and Lip@PDA-Fe-TPZ increased to about 122 nm after Lip modification (Figure S3). Compared with PDA-Fe (−10.8 mV), the Zeta potential of Lip@PDA-Fe was −18.7 mV, which was more negative after Lip modification. After further loading the electronegative drug TPZ, the Zeta potentials of PDA-Fe-TPZ and Lip@PDA-Fe-TPZ are −25.2 mV and −33.2 mV, respectively (Figure S4), meaning the successful loading of the electronegative TPZ [40]. The physiological stability of prepared nanoparticles was proved by well dispersion in water, phosphate buffered saline (PBS) and dulbecco's modified eagle medium (DMEM, contains 10% FBS) after 48 h (Figure S5). To further examine the long-term stability of Lip@PDA-Fe-TPZ, Lip@PDA-Fe-TPZ was dispersed in the above solution for 7 days, and the particle size was monitored by DLS (Figure S6 and Table S1). It was found that the particle size only slightly increased within 7 days, indicating the good long-term stability of Lip@PDA-Fe-TPZ.

To further confirm the successful loading of TPZ and Lip modification, the Fourier transform infrared (FTIR) spectrum and Ultraviolet–visible (UV–vis) spectrophotometer measurements were performed. FTIR spectrum of Lip@PDA-Fe-TPZ not only showed the characteristic peaks of N–O in TPZ (1360 cm^{-1} and 1100 cm^{-1}) [41], but also showed the characteristic peaks of the stretching vibration of

C=O (1730 cm^{-1}) and P=O (1220 cm^{-1}) bonds of Lip [42], suggesting the successful loading of TPZ and modification of Lip. The UV–vis spectrum of PDA-Fe-TPZ and Lip@PDA-Fe-TPZ showed the characteristic absorption peaks of TPZ at 269 nm and 460 nm [41,42] (Figure S7), reverifying the loading of TPZ. We used X-ray photoelectron spectroscopy (XPS) to analyze the valence state of Fe in Lip@PDA-Fe-TPZ. The Fe 2p spectrum of Lip@PDA-Fe-TPZ showed peaks at 709.34 eV, 712.07 eV, 721.90 eV, 725.47 eV, correlating to Fe(II) (2p$_{3/2}$), Fe(III) (2p$_{3/2}$), Fe (II) (2p$_{1/2}$) and Fe(III) (2p$_{1/2}$), respectively. The peak area ratio of Fe(III) to Fe(II) is 3.46:1, indicating that most of Fe in Lip@PDA-Fe-TPZ is Fe (III). The Fe(II) on the nanoparticles are mainly due to the reduction of Fe(III) during the synthesis of PDA [43–45].

Releasing sufficient of iron ions and TPZ is important for ferroptosis and chemotherapy. The loading and release behavior of TPZ and Fe ions in different buffer solutions were measured by UV–vis spectrophotometer and inductively coupled plasma-mass spectrometry (ICP-MS) testing, respectively. The contents of iron in PDA-Fe, Lip@PDA-Fe, PDA-Fe-TPZ and Lip@PDA-Fe-TPZ were 34.6 μg/mg, 27.6 μg/mg, 32.2 μg/mg and 28 μg/mg, respectively, by ICP-MS analysis. The drug loading and release of TPZ on the nanosystem were detected by UV–vis. The loading efficiency and encapsulation efficiency of TPZ on Lip@PDA-Fe-TPZ were 13.53% and 56.66%, respectively. The release percentage of TPZ and Fe ions from Lip@PDA-Fe-TPZ nanoliposomes under neutral

(pH7.4) condition were relatively low, while under acidic conditions became higher, especially in the presence of H_2O_2. In the condition of pH5.0 with 100 μM H_2O_2, the final release percentage of TPZ and Fe was 54.4% and 38.4%, respectively (Fig. 1E and F). These results suggested that Lip@PDA-Fe-TPZ may serve as a drug delivery system with low pH and endogenous H_2O_2 responsiveness, thus reducing damage to normal tissues. In addition, compared with the release of PDA-Fe-TPZ nanoparticles (Figures S8 and S9), the period for TPZ release to reach the maximum concentration was significantly increased after Lip modification, indicating that Lip could delay the release of drugs.

2.2. ROS detection

Methylene blue (MB) could be oxidized and degraded to colorless products by •OH, resulting a decrease in absorbance of solution at 664 nm. Figure S11A showed that H_2O_2 alone cannot degrade MB. However, compared with the control group, the maximum absorbability values of PDA-Fe, Lip@PDA-Fe, PDA-Fe-TPZ and Lip@PDA-Fe-TPZ with 10 mM H_2O_2 were significantly reduced (Fig. 2A and Figure S10), indicating that these nanoparticles could produce a large amount of •OH *via* Fenton reaction in 1 h. Moreover, it can be observed that the generation of •OH

is independent of TPZ. In order to further explore the effect of Lip modification on •OH under different H_2O_2 and pH conditions, PDA-Fe and Lip@PDA-Fe nanoparticles were selected as experimental groups. It should be pointed out that in the absence of H_2O_2, the nanoparticles can also trigger the degradation of MB. This is mainly due to the generation of H_2O_2 by PDA nanoparticles [46], which undergoes a Fenton reaction with iron ions on the nanoparticles to generate •OH. Therefore, using PDA nanoparticles as a drug carrier can increase the H_2O_2 level of tumors and enhance the ferroptosis effect. The effect of Lip modification on •OH production under different H_2O_2 and pH conditions were further explored. With the increase of H_2O_2 concentration, the maximum absorption of MB solution of PDA-Fe and Lip@PDA-Fe decreased gradually, indicating that high H_2O_2 concentration has a promoting effect on •OH production (Fig. 2B and C). Terephthalate (TA) reacts with •OH to produce fluorescent product 2-hydroxyterephthalic acid (TAOH) (315 nm excitation, 425 nm emission), which is used to explore •OH production under different pH conditions. The fluorescence intensity of PDA-Fe and Lip@PDA-Fe increased significantly at pH5.0, compared with pH6.5 and pH7.4 conditions (Fig. 2D). As shown in Fig. 2E, •OH can be captured by 5,5-dimethyl-1-pyrroline N-oxide (DMPO) and detected by an electron spin resonance (ESR) instrument, and the clear
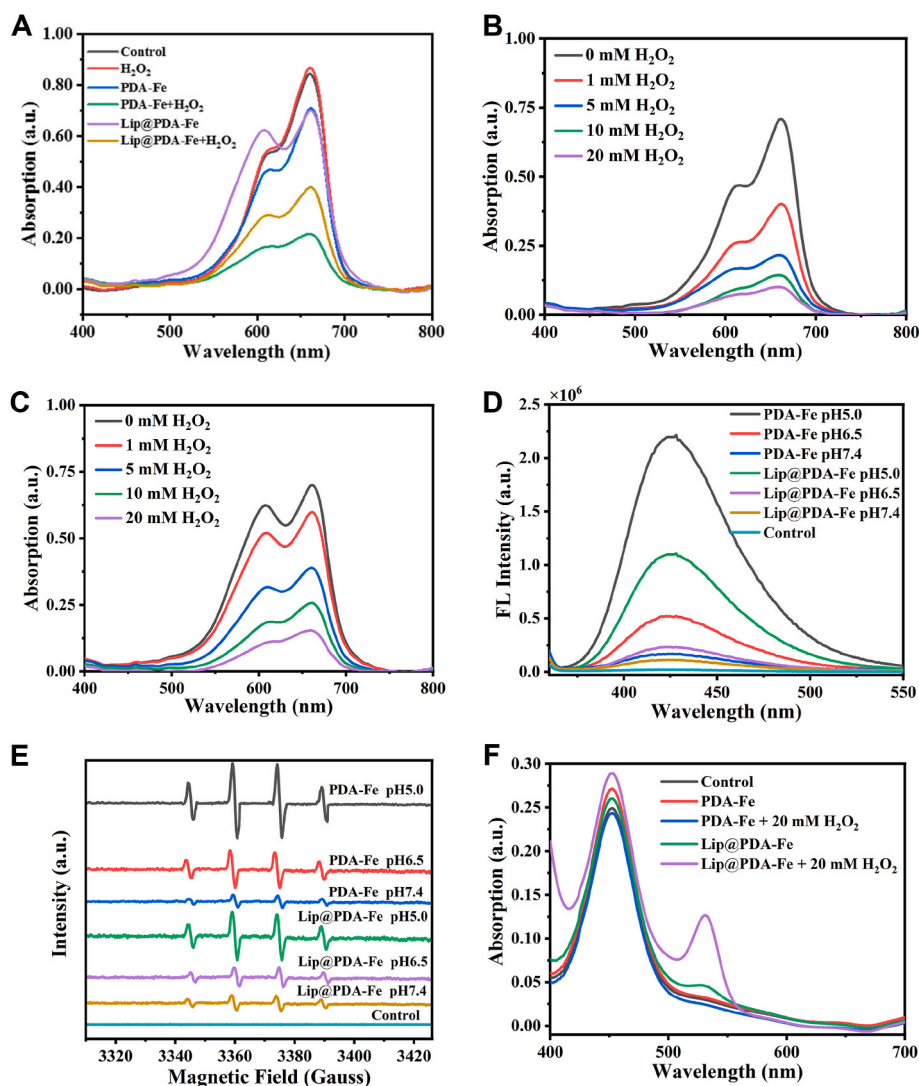
Fig. 2. Production of •OH and LPO under various conditions. (A) The degradation curves of MB after treatment with PDA-Fe, Lip@PDA-Fe with or without 10 mM H_2O_2 for 1 h. The degradation curves of MB after treatment with PDA-Fe (B) and Lip@PDA-Fe (C) in various concentration of H_2O_2. The TA fluorogram (D) and ESR spectra (E) of PDA-Fe and Lip@PDA-Fe in different pH conditions. (F) UV–vis spectrum of different treatment groups based on the TBA chromogenic method for LPO determination.

ESR signals with intensity ratio of 1:2:2:1 were obtained, which showed the same result as TA fluorescence test. The above results indicated that iron-loaded nanoparticles need abundant H_2O_2 and low pH to produce •OH, which happens to coincide with the tumor microenvironment (TME). Therefore, the synthesized nanoparticles contribute to produce large amounts of •OH in tumor cells for subsequent anti-tumor therapy.

It is worth noting that the detection results of •OH generation by MB degradation, TA fluorescence and ESR signal indicated that the •OH level of Lip@PDA-Fe is significantly lower than that of PDA-Fe under the same conditions. To explore whether •OH was consumed by reacting with modified Lip, thiobarbituric acid (TBA) chromogenic method was utilized to detect the production of lipid peroxides by UV–vis spectrophotometer. Malondialdehyde (MDA) is a commonly indicator for LPO detection, which can react with TBA in the temperature more than 95 °C and form red MDA-TBA adduct with characteristic absorption peak at 539 nm under acidic condition [47]. As shown in Fig. 2F, PDA-Fe without Lip introduction cannot produce LPO regardless of the presence or absence of H_2O_2. For Lip@PDA-Fe, there was a low strength absorption peak at 539 nm in the absence of H_2O_2, indicating that the synthesized Lip is unsaturated liposome. However, the formation of lipid peroxides MDA by •OH attacking Lip was confirmed by an obvious absorption peak for Lip@PDA-Fe in the presence of H_2O_2. The above results manifested that Lip modification could *in situ* transform •OH into stable LPO to avoid the rapid annihilation of •OH, which has the potential to enhance the combined treatment of cell ferroptosis and chemotherapy.

2.3. Cellular uptake

For the cellular uptake study, we labeled the nanoparticles (PDA-Fe-TPZ and Lip@PDA-Fe-TPZ) with fluorescent dye Rhodamine B (RhB).

The 4T1 cells were incubated for 0, 2, 4, 6 and 8 h under various treatments, and fluorescence intensity was quantitatively detected by multifunctional enzyme marker and observed by fluorescence microscope. It can be seen from Figure S11, within 6 h of incubation, the intracellular fluorescence intensity increased gradually. These results indicated that nanoliposoms can be uptaken by cells. After incubation for 6 h, the fluorescence intensity reached the maximum value, indicating that the uptake of nano-liposomes by cells reached the peak.

2.4. Cell cytotoxicity

MTT assay was used to evaluate the effect of intracellular combination therapy *in vitro* to understand the potential toxicity of Lip@PDA-Fe-TPZ nanoliposomes to cells. The cell viabilities of mouse embryonic fibroblast (3T3) cells co-incubated with PDA-Fe, Lip@PDA-Fe, PDA-Fe-TPZ and Lip@PDA-Fe-TPZ for 24 h were all higher than 80%, indicating that the cytotoxicity of nanoparticles to normal cells could be ignored (Fig. 3A). However, these nanoparticles have concentration-dependent cytotoxicity to mouse breast cancer (4T1) cells (Fig. 3B). Specifically, on the one hand, the addition of Lip increased the cytotoxicity of PDA-Fe, and the cell viabilities of 4T1 cells decreased from 84.3% (PDA-Fe) to 69.5% (Lip@PDA-Fe) at 100 μg/mL. This may be attributed to the transformation of •OH and accumulation of LPO *via* destructive chain reaction of lipid peroxidation induced by modified Lip. On the other hand, lipid peroxidation requires the participation of O_2, resulting in more hypoxic microenvironment of tumor cells. Compared with the cell viabilities of PDA-Fe-TPZ (58.6%), that of Lip@PDA-Fe-TPZ decreased to 33.4% at 100 μg/mL because TPZ cytotoxicity was activated by increased hypoxia. To further explore the cell cytotoxicity of the nanoparticles, living cells were stained with Calcein-AM and dead/late apoptotic cells were stained with propidium iodide (PI), which then
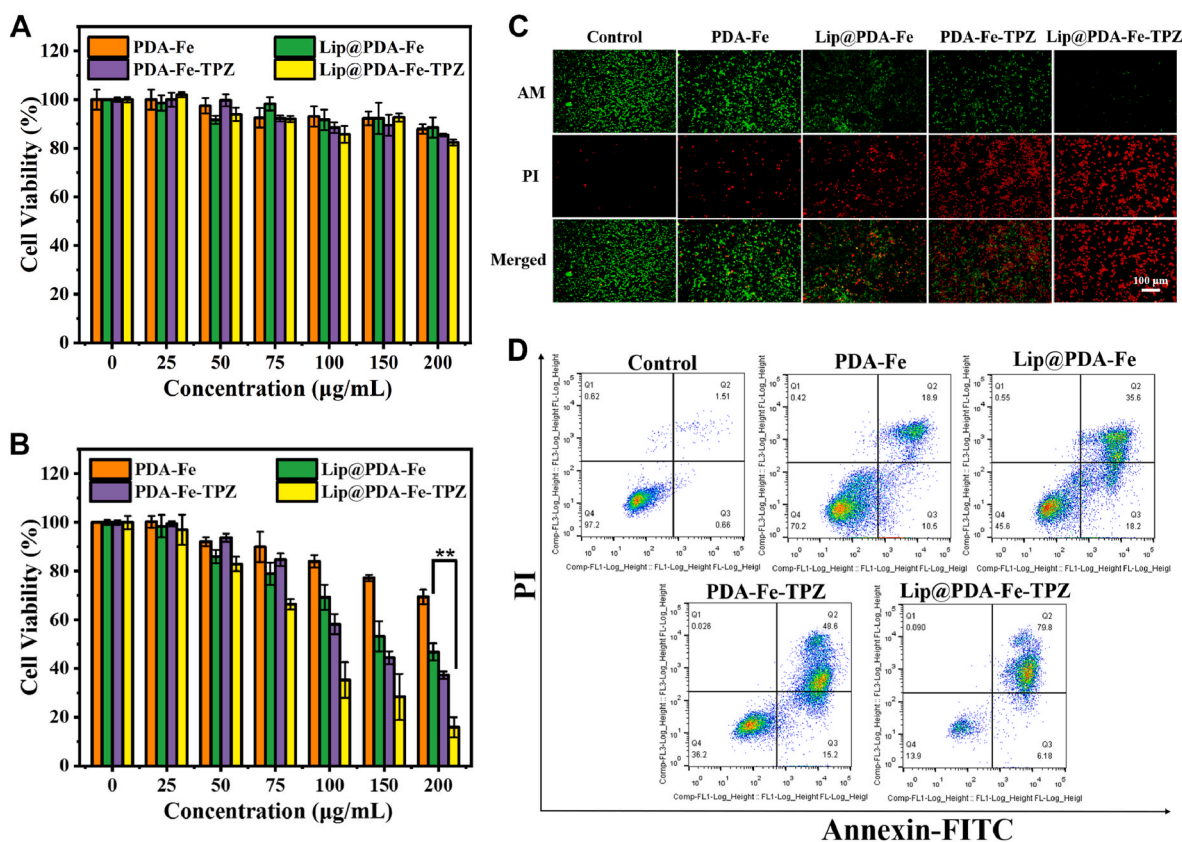

Fig. 3. *In vitro* cell cytotoxicity. Cell viability of 3T3 cells (A) and 4T1 cells (B) incubation with PDA-Fe, Lip@PDA-Fe, PDA-Fe-TPZ and Lip@PDA-Fe-TPZ after 24 h with different nanoparticles concentration. (C) Calcein-AM/PI straining of 4T1 cells after various treatments. (D) Determination of apoptosis in 4T1 cells by flow cytometry after various treatments.

assessed using fluorescence microscopic imaging. Green fluorescence (live cells) in the 4T1 cells incubated with Lip@PDA-Fe-TPZ was much lower than that in the other treatment groups due to the synergistic effect of ferroptosis and hypoxia cascade activation chemotherapy (Fig. 3C). In addition, the flow cytometric analysis was utilized by staining 4T1 cells with annexin V-FITC and PI. The results were consistent with MTT assay, and the group treated with Lip@PDA-Fe-TPZ nanoliposomes has the lowest cell survival rate (31.8%) (Fig. 3D). Compared with the good cytotoxic effect of Lip@PDA-Fe-TPZ in tumor cells, minimal cytotoxic can be found in normal cells. This different is due to the low H_2O_2 level, high level of O_2 concentrations and pH value in normal cells, which could not activate hypoxia-activated prodrug TPZ and would not produce ●OH to induce LPO. Cytotoxicity results suggested that modified Lip acts as an effective "bridge" to connect and promote ferroptosis and chemotherapy.

2.5. In vitro hypoxia studies

Lipid peroxidation requires O_2 and the activation of TPZ is sensitive to the hypoxia degree of tumor cells, thus, O_2 is an important influencing factor of cell death induced by Lip@PDA-Fe-TPZ. To further explore the effect of O_2, an AnaeroPack-Anaero was used to create the hypoxic environment. In normal culture environment, TPZ had low cytotoxicity to cells (Fig. 4A). However, the dose-dependent toxicity of TPZ was

shown in the hypoxic environment. In fact, TPZ can be activated by various intracellular reductases to produce cytotoxic free radical intermediate [1], which tends to be oxidized rapidly into the non-toxic parent molecule in the presence of O_2. Whereas in the absence of O_2, the highly reactive TPZ free radicals snatch hydrogen atoms from the biomacromolecules around them and lead to structural damage of cells. Fig. 4B showed the viabilities of cells treated with different concentration of nanoparticles for 24 h under hypoxic condition. The cell viability of 4T1 cells incubated with 100 μg/mL Lip@PDA-Fe was 69.5% under normal culture condition, but increased to 76.7% under hypoxic culture condition, which may be due to inadequate lipid peroxidation reaction without adequate O_2 support. In addition, the cell viabilities of PDA-Fe-TPZ and Lip@PDA-Fe-TPZ decreased significantly under hypoxic condition, which further indicating that the activation of TPZ requires the creation of hypoxic environment.

To prove that the addition of Lip could enhance hypoxic environment of tumor cells and activate TPZ cytotoxicity, the intracellular hypoxic level was detected by hypoxyprobe-1 probe, which can produce red fluorescence in a hypoxic state (Fig. 4D). The obvious red fluorescence of Lip@PDA-Fe and Lip@PDA-Fe-TPZ meant that the degree of hypoxia in tumor cells was improved by Lip modification. According to the quantification of red fluorescence intensity by flow cytometry (Fig. 4C), the degree of hypoxia in cells treated with Lip@PDA-Fe-TPZ was 2.4 times higher than that of PDA-Fe-TPZ. We also provided
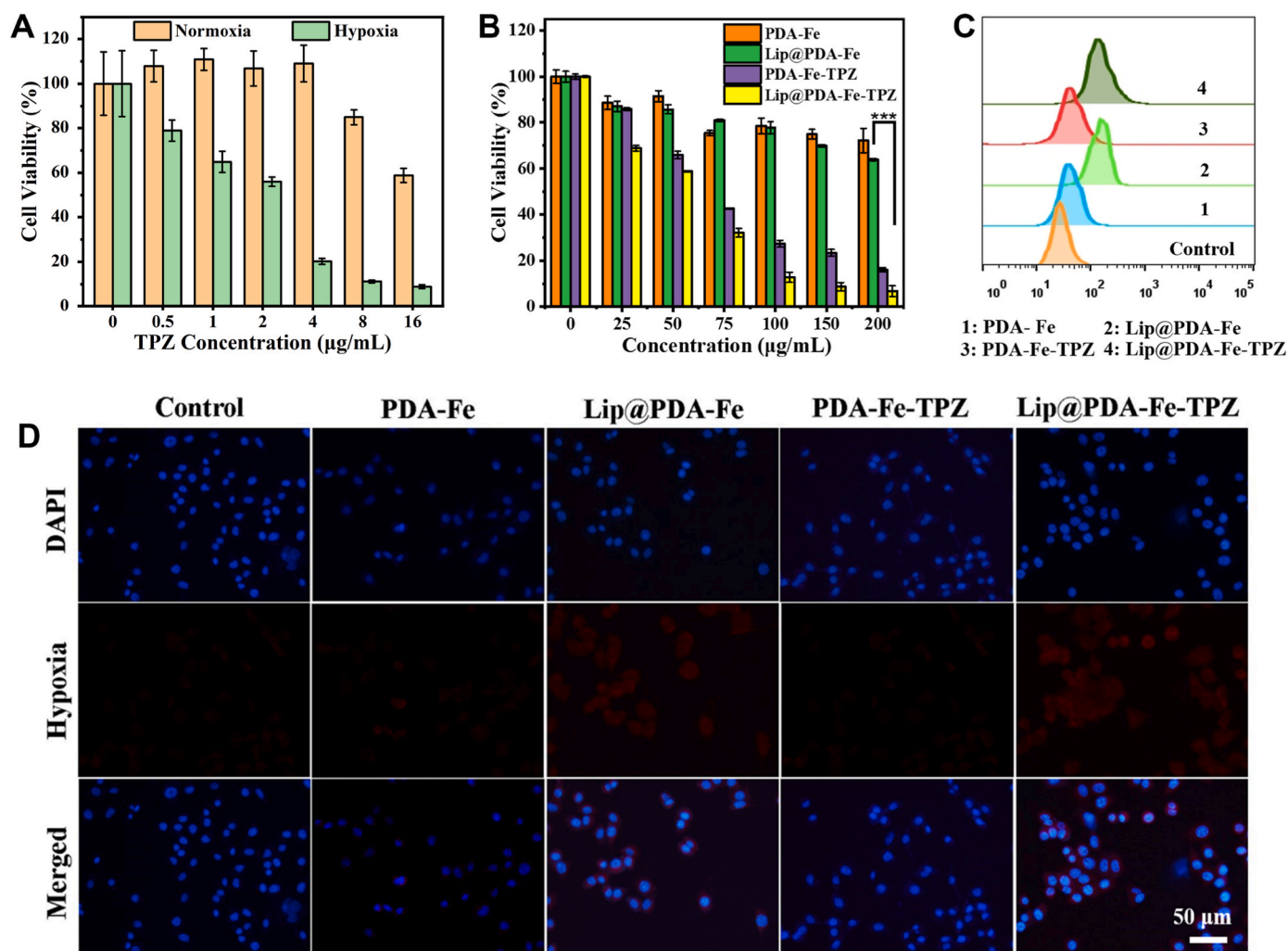

Fig. 4. (A) Cell viability of 4T1 cells treated with TPZ under normal oxygen and hypoxic conditions. (B) Cell viability of 4T1 cells treated with PDA-Fe, Lip@PDA-Fe, PDA-Fe-TPZ and Lip@PDA-Fe-TPZ under hypoxic condition. (C) Flow cytometry and (D) fluorescence images of hypoxyprobe-1 probe labeled 4T1 cells incubated with PDA-Fe, Lip@PDA-Fe, PDA-Fe-TPZ and Lip@PDA-Fe-TPZ.

images of Calcein-AM/PI straining of 4T1 cells after 24 h treatment with 200 μg/mL nanoparticles under hypoxic culture condition, and the results were consistent with those of MTT assay (Figure S12). Therefore, Lip modification and TPZ load enable Lip@PDA-Fe-TPZ as a positive feedback amplifier to take advantage of the side effects of increased hypoxia of tumor cells caused by lipid peroxidation for effective synergistic therapy.

2.6. In vitro ROS detection

The effect of Lip modification on the generation of intracellular stress levels of ROS was investigated by 2′,7′-dichlorodihydrofluorescein diacetate (DCFH-DA) detection probe. The non-fluorescent DCFH-DA probe is hydrolyzed by cell esterase to generate 2′,7′-dichlorodihydrofluorescein (DCFH), which is rapidly oxidized by ROS to generate strong fluorescence product 2′,7′-dichloro-fluorescein (DCF). As shown in Fig. 5A, 4T1 treated with Lip@PDA-Fe and Lip@PDA-Fe-TPZ nanoliposomes exhibited stronger fluorescence intensity than that of PDA-Fe and PDA-Fe-TPZ nanoparticles. The results of flow cytometry were consistent with those of fluorescence microscopy (Fig. 5B). The fluorescence intensity of 4T1 cells treated with Lip@PDA-Fe was 2.6 times than that of PDA-Fe, which can be ascribed to the lipid peroxidation.

To confirm that Lip modification can promote lipid peroxidation and ferroptosis in tumor cells, the content of MDA, the final product of lipid peroxidation, was detected under normal oxygen and hypoxic conditions (Fig. 5C). The MDA content of cells treated with Lip@PDA-Fe and

Lip@PDA-Fe-TPZ increased obviously compared with that of PDA-Fe and PDA-Fe-TPZ nanoparticles, which meant that the introduction of Lip significantly enhanced lipid peroxidation. In addition, compared with normal oxygen condition, MDA content decreased under hypoxic condition, which reprove that O_2 is an important substrate of lipid peroxidation. From this figure we also noticed that whether in PDA-Fe or Lip@PDA-Fe, the introduction of TPZ did not significantly alter the production of MDA, indicating that TPZ would not weaken the effect of nanoparticles-induced ferroptosis. These results indicated that our proposed strategy of introducing Lip to promote lipid peroxidation and cause O_2 consumption is a feasible and effective method, which can further enhance ferroptosis and activate the cytotoxicity of TPZ. Glutathione (GSH) depletion, glutathione peroxidase 4 (GPX4) inactivation, and accumulation of iron-dependent lipid peroxides are well known to cause ferroptosis [48–51]. The activity of 4T1 cells treated with ferroptosis inhibitors and inducer were measured to explore the process of ferroptosis.

By examining the effects of different ferroptosis inhibitors and promoters on the activity of 4T1 cells treated with nanoliposomes, the mechanism of tumor cell death was explored (Fig. 5D). The activity of 4T1 cells treated with PDA-Fe and Lip@PDA-Fe was partially increased with the addition of iron chelators deferoxamine (DFO), suggesting that iron ions play an important role in inducing ferroptosis. On the contrary, after the addition of DFO, cell activity showed a decreasing trend treated with PDA-Fe-TPZ and Lip@PDA-Fe-TPZ, which may be due to the fact that DFO can also be utilized as an inducer for cell hypoxia, which will
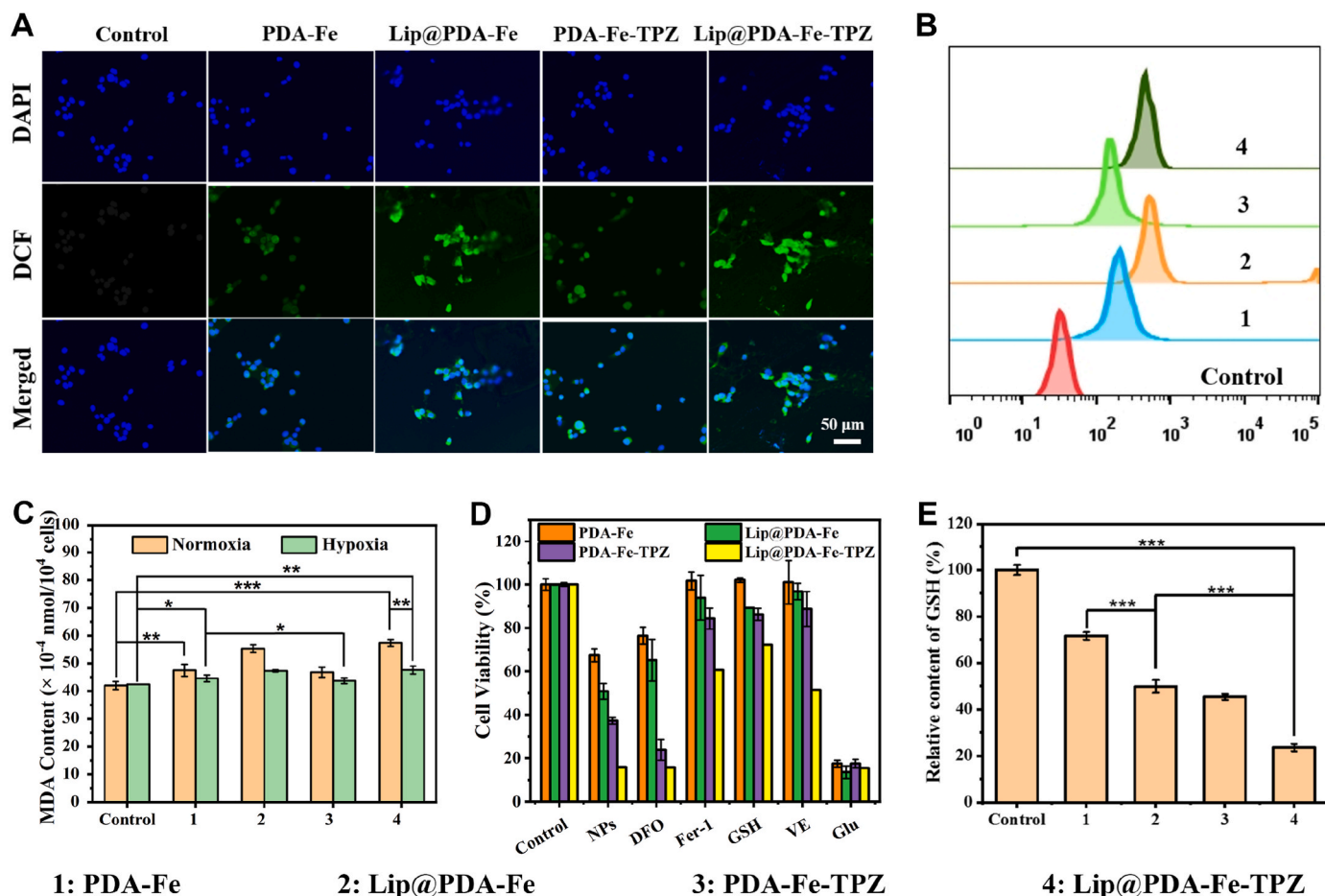

1: PDA-Fe   **2: Lip@PDA-Fe**   **3: PDA-Fe-TPZ**   **4: Lip@PDA-Fe-TPZ**

Fig. 5. (A) Fluorescence images and (B) flow cytometry of DCFH-DA labeled 4T1 cells incubated with PDA-Fe, Lip@PDA-Fe, PDA-Fe-TPZ and Lip@PDA-Fe-TPZ. (C) Detection of the LPO level in 4T1 cells treated with PDA-Fe, Lip@PDA-Fe, PDA-Fe-TPZ and Lip@PDA-Fe-TPZ under normal oxygen and hypoxic conditions by MDA assay kit. (D) Cell viability of 4T1 cells treated with PDA-Fe, Lip@PDA-Fe, PDA-Fe-TPZ, Lip@PDA-Fe-TPZ with the addition of ferroptosis-related compounds. (E) The GSH content of 4T1 cells under various treatments in 200 μg/mL for 24 h. Data represent mean ± SD of three independent experiments. Significances are marked as *P < 0.05, **P < 0.01, and ***P < 0.001.

aggravate intracellular hypoxia and lead to stronger cytotoxicity of TPZ activation. The addition of ferroptosis inhibitor Ferrostatin-1 (Fer-1), GSH and the lipophilic antioxidants Vitamin E (VE) significantly inhibit ferroptosis [52–54], suggesting that the synthesized nanoliposomes can induce the internal mechanism of ferroptosis, namely increased lipid peroxidation and GSH consumption. The 4T1 cells were incubated with Lip@PDA-Fe-TPZ (100 μg/mL), PBS for 12 h, and then we used the transmission electron microscopy (TEM) to observe morphological changes. The TEM images showed that 4T1 cells treated with Lip@PDA-Fe-TPZ for 12 h had shrunken mitochondria with decreased cristae (Figure S13). These results were in agreement with the typical cell damage caused by ferroptosis. Moreover, we studied the intracellular GSH level of 4T1 cells treated with nanoparticles (200 μg/mL) for 24 h, to further confirm their ferroptosis process. As shown in Fig. 5E, the cells treated with nanoparticles all show a lower GSH level compared to that of control group, and the GSH content of 4T1 cells treated with Lip@PDA-Fe-TPZ declined to 23.47% compared to that of 4T1 cells (control group). These results showed that the mechanism of cancer cell death induced by Lip@PDA-Fe-TPZ was ferroptosis.

2.7. Antitumor effect in vivo

4T1 tumor-bearing mice were used as experimental subjects to observe the combined antitumor therapy effect in vivo. When the tumor volume reached 100 mm^3, the mice were randomly divided into five groups and treated with PBS, PDA-Fe, Lip@PDA-Fe, PDA-Fe-TPZ and Lip@PDA-Fe-TPZ. The relative tumor volume changes of mice were shown in Fig. 6A. Tumor growth was relatively slow with the treatment of Lip@PDA-Fe and PDA-Fe-TPZ, suggesting that the antitumor therapy

based on both ferroptosis or TPZ-mediated chemotherapy can play a good antitumor effect. The Lip@PDA-Fe-TPZ exhibited the most significant antitumor effect as expected, demonstrating that ferroptosis and TPZ activity for chemotherapy were enhanced by Lip introduction. The tumor photos during treatment and tumor anatomical results after 14 days with different treatment can intuitively show the tumor treatment effect, which is consistent with the tumor growth curves (Fig. 6D and E). H&E staining was utilized to further explore the therapeutic effects of various treatments (Fig. 6F). Compared with other treatment groups, most cells lost membrane integrity and cytoplasmic nucleus shrinkage after the treatment of Lip@PDA-Fe-TPZ.

In vivo lipid peroxidation level was evaluated by detecting MDA content in tumor tissues after different treatments. The MDA content of tumor tissue treated with Lip@PDA-Fe and Lip@PDA-Fe-TPZ was higher than that of other treatments (Fig. 6B). In particular, MDA content of Lip@PDA-Fe-TPZ treatment group was 1.36 times that of PBS, indicating that synthesized nanoliposomes could induce lipid peroxidation in tumor tissues. GPX4 is a selenoprotein that specifically catalyzes GSH to convert cytotoxic lipid peroxides into nontoxic lipid alcohols, which plays an important role in regulating cell ferroptosis. GPX4 protein expression in tumor quantified by western blot analysis and quantitative analysis was measured to determine the relationship between different treatment methods and ferroptosis effect in vivo (Fig. 6C). It was observed that GPX4 was highly expressed in the PBS group, while expression of GPX4 decreased significantly after treatment with Lip@PDA-Fe and Lip@PDA-Fe-TPZ. The results were consistent with MDA content in tumor tissue, which further confirmed that the introduction of Lip enhanced the production of lipid peroxides to induce higher ferroptosis in tumor.
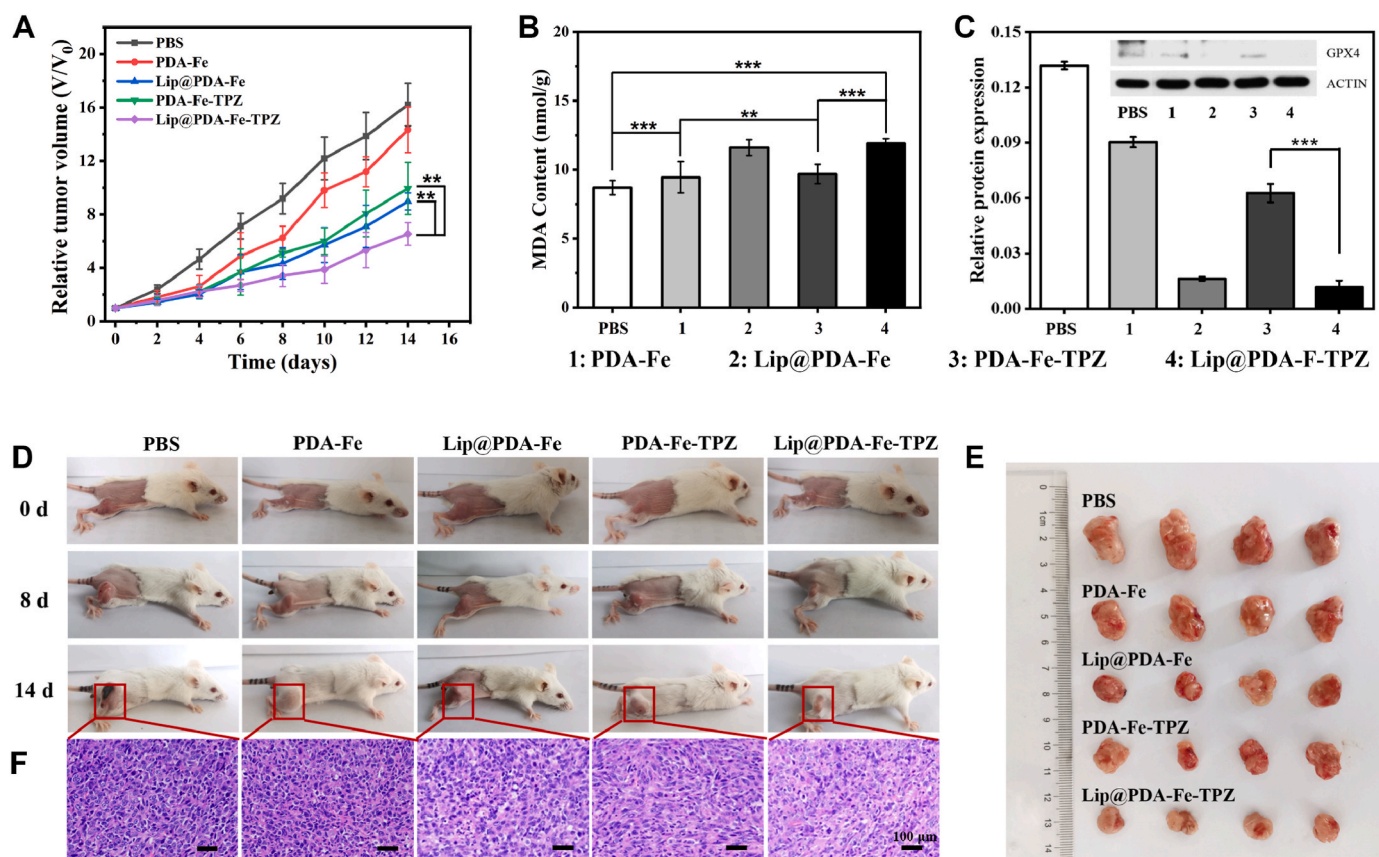

Fig. 6. (A) Tumor growth curves of mice with different treatment. (B) MDA contents of tumor tissues with different treatment. (C) Western blot analysis and quantitative analysis of GPX4 in tumor tissues with different treatment. (D) The digital photographs of mice in all five groups at day 0, day 8 and day 14. (E) Photographs at 14th day of tumors after various treatments and (F) H&E-stained images of tumor region. Significances are marked as *P < 0.05, **P < 0.01, and ***P < 0.001.

2.8. In vivo biosafety

Blood compatibility, blood biochemistry indexes and organ slicing were analyzed to systematically examine the *in vivo* biosafety of synthetic nanoparticles. There was no significant change in body weight throughout the antitumor experiments (Fig. 7A). The hemolysis rates of all prepared nanoparticles were less than 8% after 24 h treatment at a concentration of 500 μg/mL, indicating the good biocompatibility of the synthesized nanoparticles (Fig. 7B). Blood biochemical indexes, including alkaline phosphatase (ALP), blood urea nitrogen (BUN) and creatinine (CREA) of mice were measured *via* orbital blood sampling. As shown in Figure S14, compared with PBS group, there was no significant deviation of blood biochemical indexes treated with different synthetic nanoparticles, indicating that there was no obvious liver and kidney function damage. In addition, no obviously pathological abnormalities were shown in major organs including heart, liver, spleen, lung and kidney after different treatments by H&E staining, indicating that the combination therapy has few side effects (Fig. 7C). Iron content in tumor tissues and organs was measured by ICP-MS to determine the distribution of nanoparticles *in vivo* after different treatments for 14 days (Figure S15). The iron content in tumor tissues treated with Lip@PDA-Fe and Lip@PDA-Fe-TPZ 14 days was 686 μg/g and 653 μg/g, respectively, which significantly higher than that of other treatments groups, indicating that Lip@PDA-Fe-TPZ with Lip modifications could increase the enrichment of tumor site by enhancing EPR effects.

3. Conclusions

This work reported an efficient Lip@PDA-Fe-TPZ nanoliposomes as a new strategy to improve the tumor therapy, which enhanced the
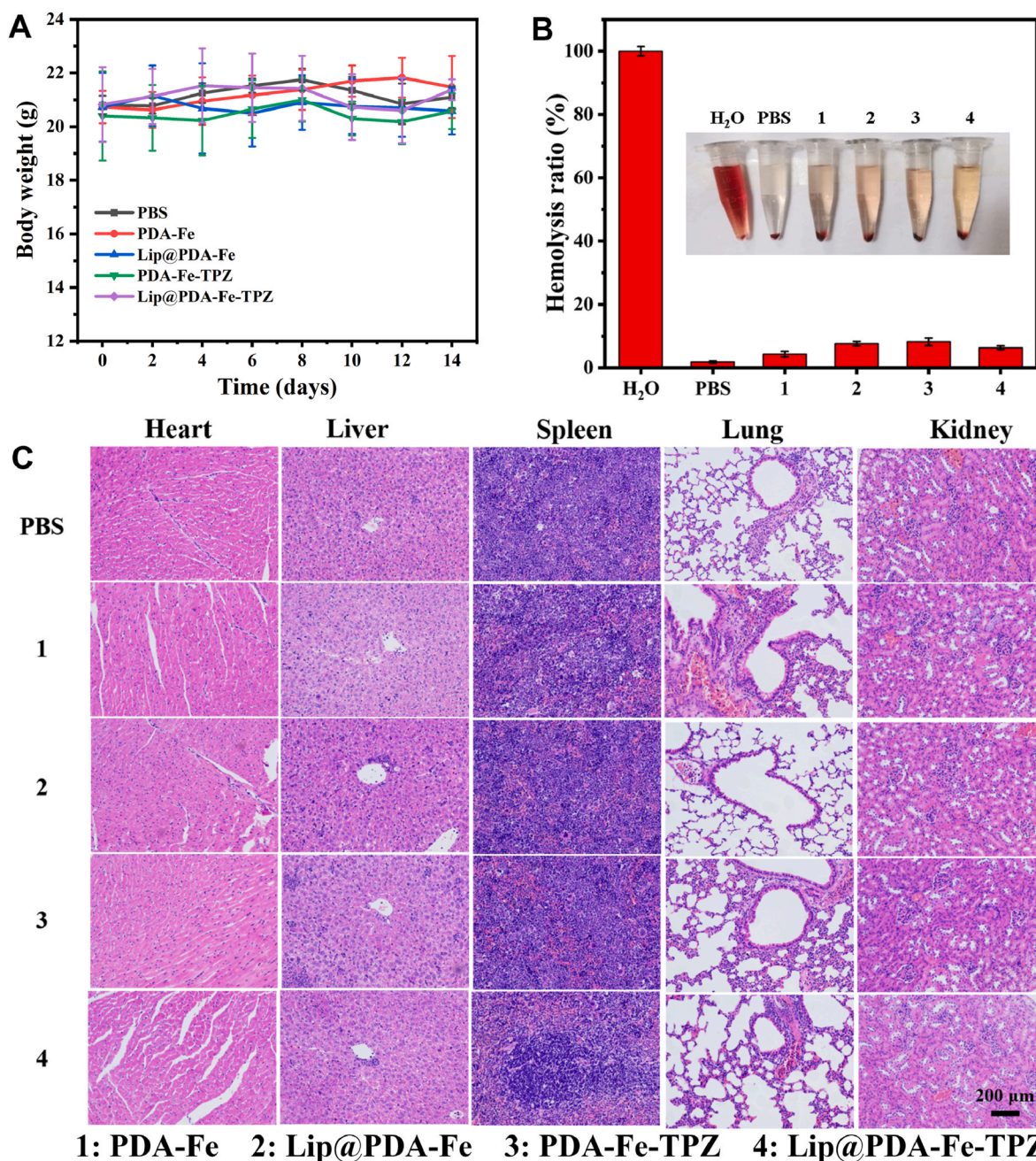
Fig. 7. (A) Body weights of mice with different treatment. (B) The hemolysis rate of H₂O, PBS, PDA-Fe, Lip@PDA-Fe, PDA-Fe-TPZ and Lip@PDA-Fe-TPZ in fresh blood. (C) H&E-stained images of the major organs of mice treated with PBS, PDA-Fe, Lip@PDA-Fe, PDA-Fe-TPZ and Lip@PDA-Fe-TPZ after 14 days.

ferroptosis effect *via* promoting lipid peroxidation. Lip@PDA-Fe-TPZ nanoliposomes with uniform size, good dispersion and physiological stability avoided the annihilation of ●OH by converting ●OH into lipid peroxides, improved the utilization rate of ROS, exacerbated the hypoxia of tumor cell, effectively activated the cytotoxicity of TPZ and realized the organic combination of ferroptosis and chemotherapy. *In vitro* and *in vivo* experiments showed that the nanoliposomes had good biocompatibility and targeted tumor specificity. The efficient antitumor function and minor side effects of Lip@PDA-Fe-TPZ nanoliposomes provide a new direction of exploring cancer treatments.

4. Experiment section

4.1. Materials

Dopamine hydrochloride (DA·HCl, 99%) and sodium hydroxide (NaOH) were purchased from Sigma-Aldrich. Acetic acid (HAc, 99%) was purchased from Xilong Chemical Co., Ltd. 1,2-distearoyl-*sn*-glycero-3-phosphatidylethanolamine (DSPE-PEG2000) and iron (III) chloride hexahydrate ($FeCl_3·6H_2O$) were supplied by Shanghai Maclean Biochemical Technology Co., Ltd. Dichloromethane ($\geq$99.5%), potassium bromide (KBr, $\geq$99.7%), nitric acid (HNO_3, $\geq$99%), methylene blue (MB), heparin sodium ($\geq$150 U/mg), hematoxylin and eosin dye were all purchased from Sangon Biotech (Shanghai) Co., Ltd. Hydrogen peroxide (H_2O_2, 30%) and 5, 5-dimethyl-1-pyrrolin-*n*-oxide (DMPO) were purchased from Thermo Fisher Scientific. Tirapazamine (TPZ) (>96%) was purchased by Dalian Meilun Biological pharmaceutical Company. Soya bean lecithin (Lip), 2-amino-2-hydroxymethylpropane-1,3-diol (Tris) and cholesterol were obtained from Sinopharm group chemical reagent Co., Ltd. Dulbecco's modified Eagle's medium (DMEM) and fetal calf serum (FBS) were acquired from Life Technologies Co., Ltd. Paraformaldehyde fixing solution (4%) and phosphate buffer (PBS) were bought from Wuhan Saiwei Biotechnology Co., Ltd. 3-(4,5-dimethylthiazol-2-thiazolyl)-2,5-diphenyl-2-H-tetrazolium bromide (MTT), 10 × PBS buffer solution, 2′,7′-Dichlorofluorescin diacetate (DCFH-DA) reactive oxygen species assay kit, cell counting kit-8 (CCK-8) kit and Annexin V-FITC apoptosis detection kit, Glutathione (GSH) detection assay kit, 2-(4-Amidinophenyl)-6-indolecarbamidine dihydrochloride (DAPI) were purchased from Beyotime Biotechnology. Vitamin E (VE) and trypsin were bought from Chengdu ruifensi Biotechnology Co., Ltd and Xiamen Yisheng Biotechnology Co., Ltd, respectively. Hypoxia detection kit, malondialdehyde (MDA) detection assay kit, dimethyl sulfoxide (DMSO) and Ferrostatin-1 (Fer-1) were obtained from Beijing solarbio science & technology Co., Ltd. Glutamic acid (Glu) was bought from Sigma-Aldrich. Glutathione (GSH) and desferrioxamine (DFO) were bought from Shanghai Aladdin Biochemical Technology Co., Ltd. AnaeroPack-Anaero and Vertical culture bag were bought by MITSUBISH GAS CHEMICAL CO., INC.

4.2. Synthesis of PDA-Fe-TPZ nanoparticles

Dopamine hydrochloride was spontaneously oxidized and polymerized in alkaline solution with pH > 7.5 to prepare PDA nanoparticles. 45 mg dopamine hydrochloride was dissolved in 120 mL deionized water containing 15 mg $FeCl_3·6H_2O$ and 10 mg TPZ with stirring for 40 min. Subsequently, 30 mL (1500 mg) Tris aqueous solution was quickly injected into the mixed solution and stirred for 2 h. The targeted nanoparticles were separated by centrifugation and washed three times with deionized water. Correspondingly, PDA-Fe nanoparticles were prepared by the same method without TPZ.

4.3. Synthesis of Lip@PDA-Fe-TPZ nanoliposomes

40 mg soya bean lecithin, 10 mg cholesterol and 10 mg distearyl phosphatidylethanolamine (MPEG2000-DSPE) were dissolved in 10 mL dichloromethane. Liposome films were then synthesized by rotary

vaporizer with a rotation speed of 50 rpm under 42 °C. The liposome films were stripped and dispersed with an ultrasonic cleaner, and then broken with an ultrasonic breaker (200 W, 2 s on, 1 s off, 2 min). The Lip@PDA-Fe-TPZ nanoliposomes were self-assembled using ultrasonic crusher (100 W, 5 s on, 5 s off, 20 min) by mixing PDA-Fe-TPZ with above Lip (the mass ratio was 1:1) and centrifuged at 10,000 rpm for 10 min. Accordingly, Lip@PDA-Fe nanoliposomes were prepared by the same method.

4.4. Characterization

The morphology of nanoparticles was observed using SEM (Hitachi, SU-70) and TEM (JEM-1400). The diameter and Zeta potential of nanoparticles were measured utilizing DLS (Nano ZS, Malvern Instruments, UK). SHIMADZU UV-1750 spectrophotometer and Nicolet iS10 FTIR spectrometer were used to determine UV–visible–NIR spectrum and Fourier transform infrared spectrum, respectively. The concentrations and release behavior of TPZ and iron were determined by UV-1750 spectrophotometer and inductively coupled plasma mass spectrometer (ICP-MS, Agilent 7500CE). The content of Lip was determined by Thermogravimetric Analysis (Netzsch TG209F1). The valence state of Fe was detected by X-ray photoelectron spectroscopy (XPS, Thermo Scientific ESCALAB Xi+).

4.5. Drug loading and release

The standard curve of TPZ was obtained by UV–vis spectrophotometer. PDA-Fe-TPZ and Lip@PDA-Fe-TPZ were centrifuged (12,000 rpm, 10 min) to collect the supernatant and calculate the TPZ content. Drug loading efficiency (DLE) = (weight of the TPZ initially added - weight of the TPZ in the supernatant)/(weight of the nanoliposomes). For TPZ release, 3 mL PDA-Fe-TPZ and Lip@PDA-Fe-TPZ were sealed in a dialysis bag (3500 Da) and dialyzed in 100 mL PBS (pH7.4, pH6.5, pH5.0 or pH5.0 + H_2O_2, respectively) at 37 °C with shaking. At the time point of 0.5, 1, 2, 4, 6, 8, 12, 24, 36 and 48 h, 3 mL dialysis solution was taken and 3 mL corresponding environmental medium solution was added. 1 mL extracellular solution was diluted at an appropriate ratio and the absorbance at 462 nm was measured by UV–vis spectrophotometer to determine the release amount of TPZ [55].

4.6. Iron ions loading and release

The standard iron ion curve was analyzed by ICP-MS with standard iron solution of 1, 3, 5 and 10 ppm to obtain iron content and iron ion release. The procedure of iron ion release experiment was the same as that of TPZ release. 1 mL extracellular dialysis solution was diluted for 10 times, and the amount of iron ion release was determined by ICP-MS.

4.7. Detection of ●OH and LPO

Methylene blue (MB) was used to detect the production of ●OH of nanoparticles in different H_2O_2 concentrations. 2 mL sample solution (250 μg/mL) and 1 mL MB solution (30 mg/L) were mixed in 2 mL H_2O_2 (0, 1, 5, 10, 20 mM) and then the mixture was kept at 37 °C for 1 h. After centrifugation for 10 min at 12,000 rpm, 3 mL supernatant was taken to test the absorbance value at 664 nm with UV–vis spectrophotometer.

The ●OH production of PDA-Fe-TPZ and Lip@PDA-Fe-TPZ nanoparticles under different pH conditions was detected based on the oxidation of terephthalic acid (TA). 300 μL sample solution, 300 μL H_2O_2 aqueous solution (10 mM) and 300 μL TA (5 mM) were transferred into 2.1 mL PBS (pH = 7.4, 6.5, 5.0). After centrifugation for 10 min at 12,000 rpm, 3 mL supernatant was tested under 315 nm excitation light after shaking 12 h at 37 °C in the dark.

Thiobarbituric acid (TBA) method was used to test the production of lipid peroxides. 100 μg/mL PDA-Fe (with/without 10 mM H_2O_2) and 100 μg/mL Lip@PDA-Fe (with/without 10 mM H_2O_2) were placed in a

constant temperature shaker at 37 °C for 24 h, followed by adding the color reagent (106 mg TBA, 20% acetic acid 30 mL and 10 mL 0.7 M NaOH solution) and keeping mixture in high temperature environment (90–100 °C) for 60 min. The mixed liquid was centrifuged and the supernatant was taken for UV–vis test.

4.8. Cell culture

3T3 and 4T1 cells were cultured in DMEM medium containing 10% fetal at 37 °C in a humidified atmosphere containing 5% CO_2. Anaero-Pack was used to create a completely hypoxic environment. The cells and AnaeroPack were placed in the culture bag and then cultured in an incubator after sealing.

4.9. Cellular uptake

1 mg/mL RhB, 4 mg 1-ethyl-3-(3-dimethylaminopropyl) carbodiimide (EDC) and 4 mg N-Hydroxysuccinimide (NHS) were mixed and stirred in a dark room for 4 h, followed by adding 10 mg PDA-Fe-TPZ and stirring for 12 h. The fluorescently labeled PDA-Fe-TPZ (PDA-Fe-TPZ-RhB) were collected by centrifuging at 12,000 rpm for 10 min and washing three times with water. The liposome encapsulated PDA-Fe-TPZ-RhB (Lip@PDA-Fe-TPZ-RhB) were prepared using ultrasonic crusher (100 W, 5 s on, 5 s off, 20 min) by mixing PDA-Fe-TPZ-RhB with Lip (the mass ratio was 1:1) and centrifuged at 10,000 rpm for 10 min.

4T1 cells (1×10^4 cells) were seeded to 96-well fluorescence black plates and incubated for 12 h. At the time nodes of 0, 2, 4, 6, and 8 h, 100 μL fluorescently labeled nanoliposomes were added for incubation, and after incubation, PBS was used for washing 3 times, followed by adding 100 μL cell lysate. Fluorescence quantification was performed with a multifunctional enzyme marker (RhB fluorescence detection parameter: Ex 555 nm, Em 585 nm).

With the same incubation method, cells were seeded to 24-well plates, then, fluorescently labeled nanoliposomes were added at different time nodes. Nucleus were stained with 2-(4-Amidinophenyl)-6-indolecarbamidine dihydrochloride (DAPI), and fluorescence images were taken with inverted fluorescence microscope.

4.10. Cellular cytotoxicity assay

In vitro cytotoxicity was evaluated by MTT assay. 4T1 cells (1×10^4 cells) were seeded to 96-well plates and incubated for 12 h. 100 μL different concentrations of samples were added and cultured for 24 h. Subsequently, cells were washed with PBS and cultured with 100 μL 10% MTT solution for 4 h. After that, MTT solution was removed and replaced by 100 μL DMSO to dissolve formazan crystals. Finally, the absorbance at 570 nm was measured with a micrometer. Similarly, 4T1 cells were cultured in a hypoxic environment created by AnaeroPack for 12 h and incubated with samples for another 24 h, and the cytotoxicity was detected by MTT method. 500 μL 4T1 cells (1×10^4/mL) were cultured in 60 mm cell culture dishes for 12 h, and then cultured with nanoparticles for another 24 h. 5 μL PI (16 mM) and 5 μL AM (4 mM) were added into 10 mL PBS. The medium was sucked out, and 1 mL Calcein AM/PI test working fluid was added. The cells were observed and photographed under a fluorescence microscope immediately after incubation at room temperature for 30 min and cleaning twice with PBS.

1 mL cell suspension (1×10^5 cells) was cultured in different nanoparticles for 24 h. The cells were centrifuged and washed with PBS, and then stained with Annexin V-FITC and PI solution successively. The cells were analyzed by flow cytometry (MoFlo, XDP, USA).

4.11. In vitro hypoxia and ROS detection

Hypoxia and ROS levels in 4T1 cells were observed by fluorescence microscopy. 5×10^4 4T1 cells were seeded onto 60 mm cell culture dishes and cultured for 12 h, followed by treating with nanoparticles for

6 h. After washing by PBS, 200 μL DCFH-DA and Hypoxyprobe-1 were added and further cultured for 20 min, subsequently. Hoechest 33,258 dye was utilized for nuclear staining. The generation of ROS and intracellular hypoxia level were detected by fluorescence microscopy and flow cytometry.

4.12. MDA evaluation and ferroptosis investigation

MDA assay kit was utilized to detect the content of LPO in 4T1 cells, which were seeded on 6-well plates (1×10^6 cells) and incubated with 500 μg/mL different treatment groups for 12 h. The cells were collected into the centrifuge tube and supernatant was removed, followed by adding 1 mL MDA extract into cell precipitation, and utilizing ultrasonic crusher (200 W, 3 s on, 10 s off, 7 min) to crush cells. Centrifugation was performed at 8500 rpm at 4 °C for 10 min, then MDA working fluid was added into supernatant and kept at 100 °C for 1 h. The absorbance of supernatant collected by centrifugation at 450 nm, 532 nm and 600 nm was measured *via* microplate reader and intracellular MDA content was calculated according to the specification of the kit instructions.

4T1 cells (1×10^4 cells) were seeded to 96-well plates and incubated for 12 h. The nanoparticles of different treatment groups were added into each well, and then immediately added media with 10 mM DFO, 1 μM Fer-1, 5 mM GSH, 2 mM Glu and 100 μM VE, respectively. The cells were then co-incubated for 24 h, followed by detecting cell viability using MTT assay.

4.13. Mitochondrial morphology

The 4T1 cells were seeded onto 10×10 cm dishes and cultured for 12 h. The cells were then incubated with PBS and Lip@PDA-Fe-TPZ (100 μg/mL) for 12 h, respectively. After incubation, the cells were collected, fixed with 2.5% glutaraldehyde solution, and then used to prepare cell sections. The TEM images of the cell sections were obtained using a JEM-1400 TEM.

4.14. Determination of intracellular GSH

4T1 cells (3×10^4 cells) were seeded into 6-well plates and cultured for 12 h. The cells were then treated with 200 μg/mL nanolipsomes for 24 h. Before intracellular GSH determination, the cells were collected *via* centrifugation and washed thoroughly with PBS. The intracellular GSH level was measured using GSH assay kits.

4.15. Animal modal establishment

Female BALB/c mice (4–6 weeks) were bought from Experimental Animal Center of Xiamen University and were utilized in accordance with to the guidelines of the State Science and Technology Commission of China. 100 μL 4T1 tumor cells (1×10^8 cells) were subcutaneously injected into BALB/c mice. The tumor-bearing mice were used for experiments when the tumor volume increased to 100 mm³.

4.16. In vivo tumor therapy

The tumor-bearing mice were randomly divided into 5 groups (4 mice in each group), 200 μL PBS, PDA-Fe, Lip@PDA-Fe, PDA-Fe-TPZ and Lip@PDA-Fe-TPZ with the dose of 20 mg/kg were injected by tail vein at 1, 3, 5, 7, 9, 11, 13 days. Tumor volume and body weight of mice were recorded continuously, and digital tumor photos were taken. After 14 days, the tumor was taken out and photographed. Meanwhile, organs including heart, liver, spleen, lung and kidney were dissected, preserved with 4% paraformaldehyde tissue fixative solution and stained with H&E. 0.4 g tumor tissues of treatments were taken for MDA content detection. After cutting into pieces and adding into 4 mL MDA extract, the tissue was broken (600 W, 3 s on, 3 s off, 3 min) with ultrasonic cell fragmentation instrument to obtain tissue homogenate. Supernatant was

centrifuged (10,000 rpm) at 4 °C for 10 min, and MDA content of tumor tissue in each group was calculated according to the specification of the kit instructions.

4.17. Hemolysis and blood biochemistry test

Hemolysis test was used to evaluate the blood compatibility of the nanoparticles. Blood was collected from eyeballs of female BALB/c mice, and red blood cells were collected by centrifugation at 4 °C for 5 min (2000 rpm). 200 μL red blood cell suspension was respectively mixed with 800 μL deionized water, PBS and 500 μg/mL PDA-Fe, Lip@PDA-Fe, PDA-Fe-TPZ and Lip@PDA-Fe-TPZ nanoparticles at 37 °C for 24 h. After centrifuging at 4 °C for 5 min (2000 rpm), 200 μL supernatant was taken and placed in a 96-well plate to determine the absorbance at 541 nm with a multifunctional microplate reader. Hemolysis percentage (HP) is calculated according to the following formula: $HP = ((A_S\text{-}A_{PBS})/(A_{H2O}\text{-}A_{PBS})) \times 100\%$. Among them, A_S, A_{H2O} and A_{PBS} represent the absorbance value of the nanoparticles, deionized water and PBS, respectively.

The effect of different treatment on liver and kidney function was evaluated by blood biochemical indexes of mice. Ten female BALB/c mice were randomly divided into five groups, including PBS, PDA-Fe, Lip@PDA-Fe, PDA-Fe-TPZ and Lip@PDA-Fe-TPZ. Eyeball blood was collected after injected for 48 h and centrifuged at 4 °C for 5 min (2000 rpm). The supernatant plasma was carefully aspirated, followed by determining the contents of alkaline phosphatase (ALP), blood urea nitrogen (BUN) and creatinine (CREA).

4.18. Determination of iron content in organs and tumor issue

The heart, liver, spleen, lung, kidney and tumor tissues of the mice with different treatment were sacrificed after 14 days. The organs and tumor tissues were weighed, cut up and nitrated with 10 mL analytical pure concentrated nitric acid. After the tissue was completely decomposed, 1 mL nitrifying solution was diluted 10 times with pure water and filtered with 450 nm filter membrane. The iron concentration in the solution was determined by ICP-MS.

CRediT authorship contribution statement

Yijun Guo: Writing – original draft, Investigation, Data curation, Conceptualization. **Huiling Luo:** Writing – original draft, Investigation, Formal analysis, Data curation. **Hairong Jiang:** Methodology. **Xinxin Liu:** Methodology. **Xinrui Long:** Visualization. **Yinuo Hou:** Methodology. **Zhou Chen:** Writing – review & editing, Supervision, Conceptualization. **Yanan Sun:** Resources. **Dongtao Ge:** Writing – review & editing, Supervision, Funding acquisition. **Wei Shi:** Writing – review & editing, Supervision, Funding acquisition, Conceptualization.

Declaration of competing interest

The authors declare that they have no known competing financial interests or personal relationships that could have appeared to influence the work reported in this paper.

Data availability

Data will be made available on request.

Acknowledgement

Appendix A. Supplementary data

Supplementary data to this article can be found online at https://doi.org/10.1016/j.mtbio.2024.101009.

References

[1] P.L. Han, L.X. Zhang, Y.Q. Fu, Y.Y. Fu, J.X. Huang, J.L. He, P.H. Ni, T. Khan, Y. Jiao, Z.X. Yang, R.H. Zhou, A dual-response drug delivery system with X-ray and ROS to boost the anti-tumor efficiency of TPZ via enhancement of tumor hypoxia levels, Nanoscale 15 (2022) 237–247, https://doi.org/10.1039/d2nr04021b.

[2] Y.Q. Du, R. Zhang, J.N. Yang, S.K. Liu, J.L. Zhou, R.X. Zhao, F. He, Y.Q. Zhang, P.P. Yang, J. Lin, A "Closed-Loop" therapeutic strategy based on mutually reinforced ferroptosis and immunotherapy, Adv. Funct. Mater. 32 (2022) 2111784, https://doi.org/10.1002/adfm.202111784.

[3] S. Goel, C.A. Ferreira, F. Chen, P.A. Ellison, C.M. Siamof, T.E. Barnhart, W.B. Cai, Activatable hybrid nanotheranostics for tetramodal imaging and synergistic photothermal/photodynamic therapy, Adv. Mater. 30 (2018) 170436, https://doi.org/10.1002/adma.201704367.

[4] G. Lei, L. Zhuang, B.Y. Gan, Targeting ferroptosis as a vulnerability in cancer, Nat. Rev. Cancer 22 (2022) 381–396, https://doi.org/10.1038/s41568-022-00459-0.

[5] C. Zhang, X.Y. Liu, S.D. Jin, Y. Chen, R.H. Guo, Ferroptosis in cancer therapy: a novel approach to reversing drug resistance, Mol. Cancer 21 (2022) 47, https://doi.org/10.1186/s12943-022-01530-y.

[6] D. Wang, Progress in the study of ferroptosis in cancer treatment: state-of-the-Art, Chem. Biol. Interact. 371 (2023) 110348, https://doi.org/10.1016/j.cbi.2023.110348.

[7] W. Qin, J.Z. Huang, C.S. Yang, Q. Yue, S.Z. Chen, M.D. Wang, S.B. Gao, X. Zhou, X.L. Zhang, Y. Zhang, Protease-Activatable nanozyme with photoacoustic and tumor-enhanced magnetic resonance imaging for photothermal ferroptosis cancer therapy, Adv. Funct. Mater. 33 (2023) 2209748, https://doi.org/10.1002/adfm.202209748.

[8] H.H. Li, M. Huang, Z.X. Wei, J.W. He, Y.N. Ma, C.X. Lu, A. Jin, Z.X. Wang, L.W. Wen, Hydrogen sulfide activatable metal-organic frameworks for Fluorescence Imaging-Guided Photodynamic Therapy of colorectal cancer, Front. Bioeng. Biotechnol. 10 (2022) 1032571, https://doi.org/10.3389/fbioe.2022.1032571.

[9] X. Dai, Y.Q. Zhu, M. Su, J.B. Chen, S. Shen, C.F. Xu, X.Z. Yang, Rigid shell decorated nanodevice with Fe/H2O2 supply and glutathione depletion capabilities for potentiated ferroptosis and synergized immunotherapy, Adv. Funct. Mater. 33 (2023) 2215022, https://doi.org/10.1002/adfm.202215022.

[10] C. Bae, H. Kim, Y.M. Kook, C. Lee, C. Kim, C. Yang, M.H. Park, Y. Piao, W.G. Koh, K. Lee, Induction of ferroptosis using functionalized iron-based nanoparticles for anti-cancer therapy, Mater, Today Bio 17 (2022) 100457, https://doi.org/10.1016/j.mtbio.2022.100457.

[11] L. Xing, X.Y. Liu, T.J. Zhou, X. Wan, Y. Wang, H.L. Jiang, Photothermal nanozyme-ignited Fenton reaction-independent ferroptosis for breast cancer therapy, J. Contr. Release 339 (2021) 14–26, https://doi.org/10.1016/j.jconrel.2021.09.019.

[12] Y.X. Yang, S.Y. Zuo, L.X. Li, X. Kuang, J.B. Li, B.J. Sun, S.J. Wang, Z.G. He, J. Sun, Iron-doxorubicin prodrug loaded liposome nanogenerator programs multimodal ferroptosis for efficient cancer therapy, Asian J. Pharm. Sci. 16 (2021) 784–793, https://doi.org/10.1016/j.ajps.2021.05.001.

[13] G. Zhu, H. Chi, M. Liu, Y. Yin, H. Diao, Z. Liu, Z. Guo, W. Xu, J. Xu, C. Cui, X.J. Xing, K. Ma, Multifunctional "ball-rod" Janus nanoparticles boosting Fenton reaction for ferroptosis therapy of non-small cell lung cancer, J. Colloid Interface Sci. 621 (2022) 12–23, https://doi.org/10.1016/j.jcis.2022.04.021.

[14] L.X. Liang, L.W. Wen, Y.Q. Weng, J.X. Song, H.H. Li, Y. Zhang, X. He, W. Zhao, M.X. Zhan, Y. Li, L.G. Lu, Y.J. Xin, C.X. Lu, Homologous-targeted and tumor microenvironment-activated hydroxyl radical nanogenerator for enhanced chemoimmunotherapy of non-small cell lung cancer, Chem. Eng. J. 425 (2021) 131451.

[15] Y. Liu, J.Z. Chen, Z. He, H.L. Luo, X.X. Liu, Y.N. Sun, D.T. Ge, X. Liu, W. Shi, Ferrocene-liposome-PEG: a robust OH/lipid peroxide nano-converter for inducing tumor ferroptosis, Biomater. Sci. 11 (2023) 542–553, https://doi.org/10.1039/d2bm01172g.

[16] L.S. Lin, S. Wang, H.Z. Deng, W.J. Yang, L. Rao, R. Tian, Y. Liu, G.C. Yu, Z.J. Zhou, J.B. Song, H.H. Yang, Z.Y. Chen, X.Y. Chen, Endogenous labile iron pool-mediated free radical generation for cancer chemodynamic therapy, J. Am. Chem. Soc. 142 (2020) 15320–15330.

[17] T. Xu, Y. Ma, Q.L. Yuan, H.X. Hu, X.K. Hu, Z.Y. Qian, J.K. Rolle, Y.Q. Gu, S. Li, Enhanced ferroptosis by oxygen-boosted phototherapy based on a 2-in-1 nanoplatform of ferrous hemoglobin for tumor synergistic therapy, ACS Nano 14 (2020) 3414–3425, https://doi.org/10.1021/acsnano.9b09426.

[18] S.Y. Chang, M.S. Tang, B.K. Zhang, D.X. Xiang, F. Li, Ferroptosis in inflammatory arthritis: a promising future, Front. Immunol. 13 (2022) 955069.

[19] J. Rodencal, S.J. Dixon, A tale of two lipids: lipid unsaturation commands ferroptosis sensitivity, Proteomics 23 (2023) e2100308, https://doi.org/10.1002/pmic.202100308.

[20] A.N. von Krusenstiern, R.N. Robson, N. Qian, B. Qiu, F. Hu, E. Reznik, N. Smith, F. Zandkarimi, V.M. Estes, M. Dupont, T. Hirschhorn, M.S. Shchepinov, W. Min, K.A. Woerpel, B.R. Stockwell, Identification of essential sites of lipid peroxidation in ferroptosis, Nat. Chem. Biol. 19 (2023) 719–730, https://doi.org/10.1038/s41589-022-01249-3.

[21] Z.F. Wu, X.Y. Liu, N.H. Deng, Z. Ren, Z.S. Jiang, Outlook of ferroptosis-targeted lipid peroxidation in cardiovascular disease, Curr. Med. Chem. 30 (2023) 3550–3561, https://doi.org/10.2174/0929867330666221111162905.

[22] H.L. Zhang, B.X. Hu, Z.L. Li, T. Du, J.L. Shan, Z.P. Ye, X.D. Peng, X. Li, Y. Huang, X. Y. Zhu, Y.H. Chen, G.K. Feng, D.J. Yang, R. Deng, X.F. Zhu, PKC beta II phosphorylates ACSL4 to amplify lipid peroxidation to induce ferroptosis, Nat. Cell Biol. 24 (2022), https://doi.org/10.1038/s41556-021-00818-3, 88-+.

[23] J. Su, Q. Zhao, Z.Z. Zheng, H.H. Wang, C.B. Bian, L.B. Meng, Y. Xin, X. Jiang, Prospective application of ferroptosis in hypoxic cells for tumor radiotherapy, Antioxidants 11 (2022) 921, https://doi.org/10.3390/antiox11050921.

[24] L.H. Liu, Y.H. Zhang, W.X. Qiu, L. Zhang, F. Gao, B. Li, L. Xu, J.X. Fan, Z.H. Li, X. Z. Zhang, Dual-stage light amplified photodynamic therapy against hypoxic tumor based on an O(2) self-sufficient nanoplatform, Small 13 (2017), https://doi.org/10.1002/smll.201701621.

[25] Q.B. Xu, G.T. Zhan, Z.L. Zhang, T.Y. Yong, X.L. Yang, L. Gan, Manganese porphyrin-based metal-organic framework for synergistic sonodynamic therapy and ferroptosis in hypoxic tumors, Theranostics 11 (2021) 1937–1952, https://doi.org/10.7150/thno.45511.

[26] Y.H. Zhang, X.L. Liu, L. Zeng, X.R. Zhao, Q.P. Chen, Y. Pan, Y. Bai, C.L. Shao, J. H. Zhang, Exosomal protein angiopoietin-like 4 mediated radioresistance of lung cancer by inhibiting ferroptosis under hypoxic microenvironment, Br. J. Cancer 127 (2022) 1760–1772, https://doi.org/10.1038/s41416-022-01956-7.

[27] M. Kunz, S.M. Ibrahim, Molecular responses to hypoxia in tumor cells, Mol. Cancer 2 (2003) 23.

[28] B. Keith, R.S. Johnson, M.C. Simon, HIF1alpha and HIF2alpha: sibling rivalry in hypoxic tumour growth and progression, Nat. Rev. Cancer 12 (2011) 9–22, https://doi.org/10.1038/nrc3183.

[29] X.M. Jing, F.M. Yang, C.C. Shao, K. Wei, M.Y. Xie, H. Shen, Y.Q. Shu, Role of hypoxia in cancer therapy by regulating the tumor microenvironment, Mol. Cancer 18 (2019) 157.

[30] D.D. Han, X. Zhang, Y.C. Ma, X.J. Yang, Z.H. Li, The development of live microorganism-based oxygen shuttles for enhanced hypoxic tumor therapy, Mater. Today Bio. 18 (2023) 100517, https://doi.org/10.1016/j.mtbio.2022.100517.

[31] W.T. Li, S.K. Liu, S.M. Dong, S.L. Gai, F.M. Zhang, Y.S. Dong, D. Yang, F. He, L. Zhong, P.P. Yang, A smart nanoplatform for synergistic starvation, hypoxia-active prodrug treatment and photothermal therapy mediated by near-infrared-II light, Chem. Eng. J. 405 (2021) 127027.

[32] D.Y. Zhao, W.Y. Tao, S.H. Li, L.X. Li, Y.X. Sun, G.T. Li, G. Wang, Y. Wang, B. Lin, C. Luo, Y.J. Wang, M.S. Cheng, Z.G. He, J. Sun, Light-triggered dual-modality drug release of self-assembled prodrug-nanoparticles for synergistic photodynamic and hypoxia-activated therapy, Nanoscale Horiz. 5 (2020) 886–894.

[33] X.B. Zhao, K. Gao, Y.P. Shi, Noncovalent theranostic prodrug for hypoxia-activated drug delivery and real-time tracking, Anal. Chem. 93 (2021) 15080–15087.

[34] E. Janczy-Cempa, O. Mazuryk, A. Kania, M. Brindell, Significance of specific oxidoreductases in the design of hypoxia-activated prodrugs and fluorescent turn off-on probes for hypoxia imaging, Cancers 14 (2022) 2686.

[35] B. Harris, S. Saleem, N. Cook, E. Searle, Targeting hypoxia in solid and haematological malignancies, J. Exp. Clin. Cancer Res. 41 (2022) 318, https://doi.org/10.1186/s13046-022-02522-y.

[36] D.C. Yang, L.F. Wen, L. Du, C.M. Luo, Z.Y. Lu, J.Y. Liu, Z. Lin, A hypoxia-activated prodrug conjugated with a BODIPY-based photothermal agent for imaging-guided chemo-photothermal combination therapy, ACS Appl. Mater. Interfaces 14 (2022) 40546–40558, https://doi.org/10.1021/acsami.2c09071.

[37] M. Ivan, M.L. Fishel, O.M. Tudoran, K.E. Pollok, X. Wu, P.J. Smith, Hypoxia signaling: challenges and opportunities for cancer therapy, Semin. Cancer Biol. 85 (2022) 185–195, https://doi.org/10.1016/j.semcancer.2021.10.002.

[38] Z. Chen, F.F. Han, Y. Du, H.Q. Shi, W.C. Zhou, Hypoxic microenvironment in cancer: molecular mechanisms and therapeutic interventions, Signal Transduct. Targeted Ther. 8 (2023) 70, 70.

[39] H. Zhang, C. Shi, F.P. Han, M.Q. Li, H. Ma, R. Sui, S.R. Long, W. Sun, J.J. Du, J. L. Fan, H.Z. Piao, X.J. Peng, Precise gliomas therapy: hypoxia-activated prodrugs sensitized by nano-photosensitizers, Biomaterials 289 (2022) 121770, https://doi.org/10.1016/j.biomaterials.2022.121770.

[40] G. Ajnai, C.C. Cheng, T.C. Kan, J.W. Lu, S. Rahayu, A. Chiu, J.S. Chang, Improving tirapazamine (TPZ) to target and eradicate hypoxia tumors by gold nanoparticle carriers, Pharm. Times 14 (2022) 847, https://doi.org/10.3390/pharmaceutics14040847.

[41] W.C. Wu, Y.Y. Pu, H.L. Yao, H. Lin, J.L. Shi, Microbiotic nanomedicine for tumor-specific chemotherapy-synergized innate/adaptive antitumor immunity, Nano Today 42 (2022) 101377, https://doi.org/10.1016/j.nantod.2022.101377.

[42] Y. Hu, S. Bai, X.Y. Fan, F.F. Zhou, B.T. Chen, S.W. Tan, H. Xu, A.Q. Pan, S.Q. Liang, Y.J. He, Autocatalytic oncotherapy nanosystem with glucose depletion for the cascade amplification of hypoxia-activated chemotherapy and H2O2-dependent chemodynamic therapy, Biomater. Sci. 10 (2022) 2358–2369.

[43] H. Liu, X. Qu, H. Tan, J. Song, M. Lei, E. Kim, G.F. Payne, C. Liu, Role of polydopamine's redox-activity on its pro-oxidant, radical-scavenging, and antimicrobial activities, Acta Biomater. 88 (2019) 181–196, https://doi.org/10.1016/j.actbio.2019.02.032.

[44] L. Du, R. Liao, H. Zhang, X. Qu, X. Hu, Redox-activity of polydopamine for ultrafast preparation of self-healing and adhesive hydrogels, Colloids Surf., B 214 (2022) 112469, https://doi.org/10.1016/j.colsurfb.2022.112469.

[45] H. Xu, X. Liu, G. Su, B. Zhang, D. Wang, Electrostatic repulsion-controlled formation of polydopamine-gold Janus particles, Langmuir 28 (2012) 13060–13065, https://doi.org/10.1021/la302394e.

[46] H. Liu, X. Qu, H.Q. Tan, J.L. Song, M. Lei, E. Kim, G.F. Payne, C.S. Liu, Role of polydopamine's redox-activity on its pro-oxidant, radical-scavenging, and antimicrobial activities, Acta Biomater. 88 (2019) 181–196, https://doi.org/10.1016/j.actbio.2019.02.032.

[47] Z. Wu, Y.J. Wang, Y.F. Wang, K.N. Zhang, Y.C. Lai, Robust and reliable detection of malondialdehyde in biological samples via microprobe-triggered surface-enhanced Raman spectroscopy, Microchem. J. 181 (2022) 107815, https://doi.org/10.1016/j.microc.2022.107815.

[48] J.S. Zheng, M. Conrad, The metabolic underpinnings of ferroptosis, Cell Metabol. 32 (2020) 920–937, https://doi.org/10.1016/j.cmet.2020.10.011.

[49] X.M. Yao, W. Li, D. Fang, C.Y. Xiao, X. Wu, M.H. Li, Z. Luo, Emerging roles of energy metabolism in ferroptosis regulation of tumor cells, Adv. Sci. 8 (2021) e2100997, https://doi.org/10.1002/advs.202100997.

[50] J. Muri, M. Kopf, Redox regulation of immunometabolism, Nat. Rev. Immunol. 21 (2021) 363–381.

[51] F.Y. Yu, X.W. Shang, Z. Wang, Y. Zhu, S.M. Chen, H. Yuan, F.Q. Hu, Drug-independent NADPH-consuming micelles collaborate with ROS-generator for cascade ferroptosis amplification by impairing redox homeostasis, Mater. Today Bio. 18 (2023) 100532, https://doi.org/10.1016/j.mtbio.2022.100532.

[52] Q. Hu, Y.F. Zhang, H.L. Lou, Z.X. Ou, J. Liu, W.T. Duan, H. Wang, Y.L. Ge, J.X. Min, F.D. Wang, Z.Y. Ju, GPX4 and vitamin E cooperatively protect hematopoietic stem and progenitor cells from lipid peroxidation and ferroptosis, Cell Death Dis. 12 (2021) 706, https://doi.org/10.1038/s41419-021-04008-9.

[53] L.B. Pontel, A. Bueno-Costa, A.E. Morellato, J. Carvalho Santos, G. Roue, M. Esteller, Acute lymphoblastic leukemia necessitates GSH-dependent ferroptosis defenses to overcome FSP1-epigenetic silencing, Redox Biol. 55 (2022) 102408, https://doi.org/10.1016/j.redox.2022.102408.

[54] Y. Xu, Y.T. Li, J.X. Li, W. Chen, Ethyl carbamate triggers ferroptosis in liver through inhibiting GSH synthesis and suppressing Nrf2 activation, Redox Biol. 53 (2022) 102349, https://doi.org/10.1016/j.redox.2022.102349.

[55] A.A. Joshi, P.P. Nerkar, Determination of proton pump inhibitors by spectrophotometric, chromatographic and by hyphenated techniques: a review, Crit. Rev. Anal. Chem. 51 (2021) 527–548, https://doi.org/10.1080/10408347.2020.1750339.